

Article

Synthesis, Structural Features and Physical Properties of a Family of Triply Bridged Dinuclear 3d-4f Complexes

Itziar Oyarzabal ^{1,*}, Estitxu Echenique-Errandonea ¹, Eider San Sebastián ¹, Antonio Rodríguez-Diéguez ², José Manuel Seco ^{1,*} and Enrique Colacio ^{2,*}

¹ Departamento de Química Aplicada, Facultad de Química, Universidad del País Vasco UPV/EHU, Paseo Manuel de Lardizabal 3, 20018 Donostia-San Sebastián, Spain; estitxu.echenique@ehu.eus (E.E.-E.); eider.sansebastian@ehu.eus (E.S.S.)

² Departamento de Química Inorgánica, Facultad de Ciencias, Universidad de Granada, Avda. Fuentenueva S/N, 18002 Granada, Spain; antonio5@ugr.es

* Correspondence: itziar.oyarzabal@ehu.eus (I.O.); josemanuel.seco@ehu.eus (J.M.S.); ecolacio@ugr.es (E.C.)

Abstract: New dinuclear M^{II}-Ln^{III} complexes of general formulas [Cu(μ-L)(μ-OAc)Ln(NO₃)₂] \cdot CH₃CN \cdot H₂O (Ln^{III} = Gd (1), Tb (2), Dy (3) and Er (4)), [Ni(CH₃CN)(μ-L)(μ-OAc)Ln(NO₃)₂] \cdot CH₃CN (Ln^{III} = Nd (5), Gd (6), Tb (7), Dy (8), Er (9) and Y (10)) and [Co(CH₃CN)(μ-L)(μ-OAc)Ln(NO₃)₂] \cdot CH₃CN (Ln^{III} = Gd (11), Tb (12), Dy (13), Er (14) and Y (15)) were prepared from the compartmental ligand *N,N'*-dimethyl-*N,N'*-bis(2-hydroxy-3-formyl-5-bromo-benzyl)ethylenediamine (H₂L). In all these complexes, the transition metal ions occupy the internal N₂O₂ coordination site of the ligand, whereas the Ln^{III} ions lie in the O₄ external site. Both metallic ions are connected by an acetate bridge, giving rise to triple mixed diphenoxido/acetate bridged M^{II}Ln^{III} compounds. Direct current (*dc*) magnetic measurements allow the study of the magnetic exchange interactions between the 3d and 4f metal ions, which is supported by density functional theory (DFT) theoretical calculations for the Gd^{III}-based counterparts. Due to the weak ferromagnetic exchange coupling constants obtained both experimentally and theoretically, the magneto-thermal properties of the less anisotropic systems (compounds 1 and 6) are also studied. Alternating current (*ac*) magnetic measurements reveal the occurrence of slight frequency dependency of the out-of-phase signal for complexes 8, 9 and 13, while complex 15 displays well-defined maximums below ~6 K.

Keywords: transition metal ions; lanthanide(III) metal ions; molecular magnetism; magneto-caloric effect



Citation: Oyarzabal, I.; Echenique-Errandonea, E.; San Sebastián, E.; Rodríguez-Diéguez, A.; Seco, J.M.; Colacio, E. Synthesis, Structural Features and Physical Properties of a Family of Triply Bridged Dinuclear 3d-4f Complexes. *Magnetochemistry* **2021**, *7*, 22. <https://doi.org/10.3390/magnetochemistry7020022>

Academic Editor: Floriana Tuna
Received: 14 January 2021
Accepted: 1 February 2021
Published: 5 February 2021

Publisher's Note: MDPI stays neutral with regard to jurisdictional claims in published maps and institutional affiliations.



Copyright: © 2021 by the authors. Licensee MDPI, Basel, Switzerland. This article is an open access article distributed under the terms and conditions of the Creative Commons Attribution (CC BY) license (<https://creativecommons.org/licenses/by/4.0/>).

1. Introduction

The design and synthesis of molecular complexes that display slow relaxation of the magnetization, i.e., single-molecule magnet behaviour (SMMs), has gained increasing attention in the past few decades [1–6]. This interest is mainly due to their potential applications, as these compounds could be used in emerging fields such as molecular spintronics, ultra-high density magnetic information storage and quantum computing [7,8]. The fundamental characteristic of SMM behaviour is the presence of an energy barrier for the reorientation of the spin of the ground state, which can be defined in terms of a large (or at least non-zero) ground spin state (*S*) and a large magnetic anisotropy (*D*).

Research efforts in the field of SMMs have shown that the use of heavy lanthanide ions (e.g., Dy^{III} and Tb^{III}) is a good strategy to obtain compounds with these unique properties, as lanthanides have large angular momentum in the ground multiplet state and, therefore, large anisotropy [9,10]. However, such complexes often display additional relaxation pathways, such as quantum tunnelling of the magnetization (QTM) or spin-phonon couplings, which lead to narrow hysteresis loops and/or the absence of slow relaxation of the magnetization without the application of an external field. Since these effects are less pronounced in 3d metal-based SMMs, hybrid 3d-4f systems appear to be

a suitable solution to the aforementioned problem [11–14]. Additionally, ferromagnetic interactions between the *d* and *f* ions can lead to an increased ground spin state, a prerequisite for the observation of SMM behaviour.

In the systems in which the magnetic interactions are not strong enough and/or the magnetic anisotropy is not large enough for the appearance of slow relaxation of the magnetization, other exciting physical phenomena such as the magneto-caloric effect (MCE) can still be studied [15]. The multiple low-lying excited and field-accessible states generated in such compounds contribute to the overall magnetic entropy, which can be modulated upon the application of an external magnetic field. Thus, hybrid *3d-4f* complexes containing isotropic Gd^{III} ions (with a calculated maximum entropy value of $R\ln(2S_{\text{Gd}} + 1)/M_{\text{Gd}} = 110 \text{ J}\cdot\text{kg}^{-1}\cdot\text{K}^{-1}$) and *3d* transition metal ions (e.g., Cu^{II} and Ni^{II}) are good candidates for solid state refrigeration.

With this in mind, in this work we prepare a novel family of triply bridged dinuclear *3d-4f* complexes and study their magnetic properties. The flexible Mannich base *N,N'*-dimethyl-*N,N'*-bis(2-hydroxy-3-formyl-5-bromobenzyl) ethylenediamine (H₂L) ligand allows the coordination of metallic ions with different sizes, leading to a series of triply bridged M^{II}-Ln^{III} dinuclear species: [Cu(μ-L)(μ-OAc)Ln(NO₃)₂] \cdot CH₃CN \cdot H₂O (Ln^{III} = Gd, Tb, Dy and Er), [Ni(CH₃CN)(μ-L)(μ-OAc)Ln(NO₃)₂] \cdot CH₃CN (Ln^{III} = Nd, Gd, Tb, Dy, Er and Y) and [Co(CH₃CN)(μ-L)(μ-OAc)Ln(NO₃)₂] \cdot CH₃CN (Ln^{III} = Gd, Tb, Dy, Er and Y).

2. Results

The reaction of H₂L with Cu(OAc)₂ \cdot H₂O and Ln(NO₃)₃ \cdot nH₂O in a CH₃CN/MeOH mixture and in 1:1:1 molar ratio led to dark green crystals of the compounds [Cu(μ-L)(μ-OAc)Ln(NO₃)₂] \cdot CH₃CN \cdot H₂O (Ln^{III} = Gd (1), Tb (2), Dy (3), Er (4)). The same reaction but using Ni(OAc)₂ \cdot 4H₂O instead of Cu(OAc)₂ \cdot H₂O, led to green crystals of the similar dinuclear complexes [Ni(CH₃CN)(μ-L)(μ-OAc)Ln(NO₃)₂] \cdot CH₃CN (Ln^{III} = Nd (5), Gd (6), Tb (7), Dy (8), Er (9), Y (10)), where the major differences between the Cu^{II} and Ni^{II}-based dimers reside in the coordination environment of the *3d* metal ions and the disposition of the ligands around them. The use of Co(OAc)₂ \cdot 4H₂O as source of metal led to the formation of dinuclear complexes with the general formula [Co(CH₃CN)(μ-L)(μ-OAc)Ln(NO₃)₂] \cdot CH₃CN (Ln^{III} = Gd (11), Tb (12), Dy (13), Er (14), Y (15)), which are isostructural to the Ni^{II} analogues (Information about the purity of the samples and the crystallographic data can be found in Tables S1–S6).

Crystal Structures

Complexes 1–4 are isostructural between them and are very similar to the Zn^{II}-Ln^{III} complexes previously reported by us [16], but contain Cu^{II} instead of Zn^{II} (Figure 1). In these complexes, the Cu^{II} and Ln^{III} ions are bridged by two phenoxido groups of the ligand and one syn-syn acetate, forming bis(phenoxido)acetate triply bridged dinuclear entities. The Cu^{II} ions are also coordinated to two nitrogen atoms from the amine groups (N1A and N2A), leading to CuN₂O₃ coordination spheres with geometries that can be considered as intermediate between square pyramid and vacant octahedron according to the SHAPE software (Table S7) [17]. The Cu–O and Cu–N distances are found in the 1.999(2)–2.146(2) and 2.017(2)–2.024(3) Å ranges, respectively, being the largest distances those corresponding to the Cu–O_{acetate} bonds (Table S5).

On the other hand, the LnO₉ coordination spheres are composed of two aldehyde oxygen atoms (O1A and O4A) of the ligand and four oxygen atoms belonging to two bidentate nitrate anions (O1C, O2C, O1D and O2D), as well as of the three bridging oxygen atoms mentioned previously. The LnO₉ spheres encompass assorted Ln–O bond distances, including short Ln–O distances in the 2.254(2)–2.290(2) Å range that correspond to the Ln–O_{acetate} bonds, intermediate Ln–O_{ligand} bond distances in the 2.326(2)–2.404(2) Å range and large Ln–O_{nitrate} distances in the 2.426(2)–2.534(2) Å range. Due to these variety on bond distances, the LnO₉ coordination spheres can be considered as intermediate between several nine-vertex polyhedral, as supported by the SHAPE software (Table S10) [17].

The intradimeric Cu–Ln distances are in the 3.353(3)–3.380(1) Å range and are greatly influenced by the lanthanide contraction as they decrease from Gd^{III} to Er^{III}, being this effect also observable in Ln–O_{ligand} and Ln–O_{acetate} bonds (Table S5).

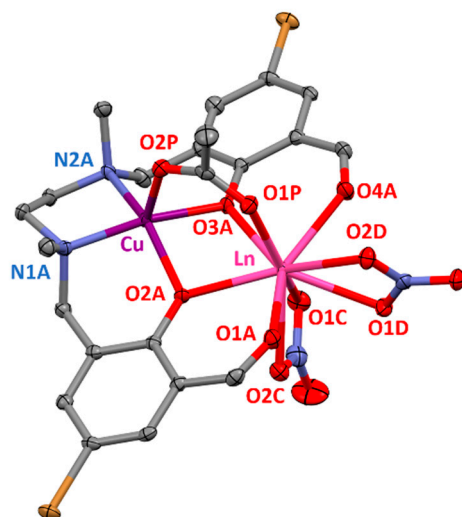


Figure 1. Perspective view of the molecular structure of **1–4**. Crystallization solvent molecules and hydrogen atoms are omitted for the sake of clarity. Colour code: N = blue, O = red, C = grey, Br = brown, Cu = purple, Ln = pink.

The average Ln–O–Cu angles are between 99.51(6) and 100.29(7)° in complexes **1–4** and, due to the acetate bridging group, the CuLn dimers show folded structures with average hinge angles in the 24.29–25.07° range (the hinge angle, β , is the dihedral angle between the O2A–Cu–O3A and O2A–Ln–O3A planes in the bridging fragment). Both aromatic rings of the ligand are almost in the same plane, forming dihedral angles ranging from 15.73 to 16.04°.

Finally, it should be mentioned that complexes **1–4** exhibit hydrogen bond interactions between the crystallization water molecules and one of the oxygen atoms of the bidentate nitrate group, one of the oxygen atoms of the acetate bridging group (O2P) and the nitrogen atom of the crystallization acetonitrile molecule (Figure S1).

Complexes **5–10** possess very similar molecular structures to that of **1–4**, but consist of Ni^{II}–Ln^{III} dinuclear units and the coordination environment of Ni^{II} ions is different to that of the Cu^{II} ions (Figure 2). In these complexes, the Ni^{II} ions are coordinated to an additional nitrogen atom (N1F) that belongs to an acetonitrile molecule and therefore, exhibit NiN₃O₃ coordination spheres. The three oxygen atoms (O2A, O3A, O1P) and consequently, the three nitrogen atoms (N1A, N2A, N1F) occupy facial (*fac*) positions in these slightly distorted coordination polyhedra. In fact, computed shape measurements indicate that NiN₃O₃ coordination spheres are found in the OC-6 ↔ TPR-6 deformation pathway and are close to the octahedral geometry (75.8–77.1%) somewhat distorted to trigonal prismatic (Table S8). The Ni–O and Ni–N bond distances are similar to each other and vary between 2.051(6)–2.136(4) Å and 2.060(5)–2.108(4) Å, respectively. The lanthanide ions show similar coordination environments as in complexes **1–4**, exhibiting rather asymmetric coordination spheres where the average Ln–O distances are in the range 2.275(2)–2.537(7) Å. As a matter of fact, the computed shape measurements relative to the ideal nine-vertex polyhedra for the LnO₉ coordination sphere are very close to those obtained for compounds **1–4** (Table S10). The average Ni^{II}–Ln^{III} distances are in the range 3.385(1)–3.437(2) Å and as expected, the average Ln–O_{ligand} bond distances steadily decrease from Nd^{III} to Er^{III} following the lanthanide contraction, with a concomitant decrease of the average Ni^{II}–Ln^{III} and Ln–O_{acetate} bond distances.

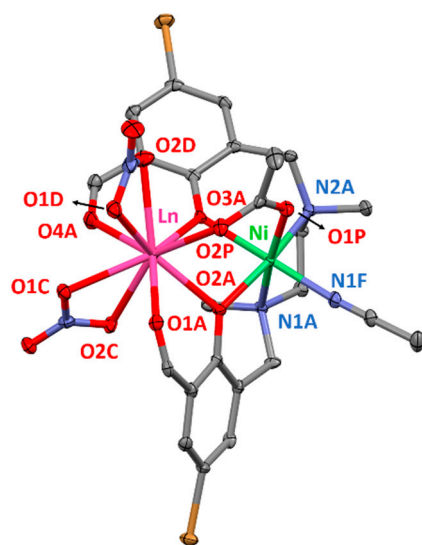


Figure 2. Perspective view of the molecular structure of **5**. Crystallization solvent molecules and hydrogen atoms are omitted for clarity. Colour code: N = blue, O = red, C = grey, Br = brown, Ni = green, Ln = pink.

The M–O–Ln angles of complexes **5–10** are similar to those found in complexes **1–4** and are in the 97.6(2)–101.99(7)° range. Compared to the Cu^{II}-based analogues, the ligand shows more twisted disposition around the metal ions, in which the dihedral angles between the two aromatic rings are in the 69.92–71.39° range. The torsion of the ligand leads to an increase in the hinge angle compared to complexes **1–4**, being in the 27.88–28.39° range.

To end up, complexes **11–15** are isostructural to complexes **5–10** but contain Co^{II} ions and crystallize in the triclinic *P*-1 space group. The CoN₃O₃ and LnO₉ coordination spheres show similar coordination environments to those found in complexes **5–10**, with 71.9–72.7% octahedral geometry for Co^{II} ions (Table S9). Bond distances and angles are also close to those found for complexes **5–10** and further discussion on the structure of these complexes will be omitted.

3. Discussion

3.1. Magnetic Properties

The temperature dependence of the magnetic susceptibility for the dinuclear Cu^{II}Ln^{III} complexes were measured on polycrystalline samples in the 5–300 K (**1**) and 2–300 K (**2–4**) temperature ranges under an applied field of 0.1 T and is given in the form $\chi_M T$ in Figure 3.

At room temperature, the $\chi_M T$ value for **1** of 8.27 cm³·K·mol⁻¹ matches very well with the expected value for non-interacting Cu^{II} ($S = 1/2$) and Gd^{III} ($S = 7/2$) ions (8.25 cm³·K·mol⁻¹ with $g = 2$). On cooling, the $\chi_M T$ product remains constant until 70 K and then increases at lower temperatures, reaching a maximum value of 9.31 cm³·K·mol⁻¹ at 5 K, pointing to the presence of ferromagnetic exchange interactions within the Cu^{II}Gd^{III} dinuclear unit. The field dependence of the molar magnetization at 2 K for compound **1** (Figure 3) shows a relatively rapid increase in the magnetization at low fields, in agreement with a high-spin state, and a rapid saturation of the magnetization that is almost complete above 3 T, reaching a value of 7.91 N μ_B at 5 T. The obtained value is in good agreement with the theoretical value for a $S_T = 4$ spin ground state (8 N μ_B for $g = 2$).

The magnetic susceptibility and magnetization data for complex **1** have been simultaneously modelled using the following Hamiltonian formula:

$$H = -JS_{\text{Cu}}S_{\text{Gd}} - zJ' \langle S_z \rangle S_z + g_e \mu_B SH \quad (1)$$

where J is the magnetic exchange pathway through the di- μ -phenoxo/*syn-syn* acetate triple bridge, $-zJ' \langle S_z \rangle S_z$ accounts for the intermolecular interactions by means of the

molecular field approximation, g_e is the average g factor, μ_B is the Bohr magneton and H is the magnetic field. The fit of the experimental susceptibility data using the full-matrix diagonalization PHI program [18] afforded the following set of parameters when fixing g to 2.0 for both ions: $J = +2.30 \text{ cm}^{-1}$ and $zJ' = -0.006 \text{ cm}^{-1}$ with $R = 2.08 \times 10^{-5}$.

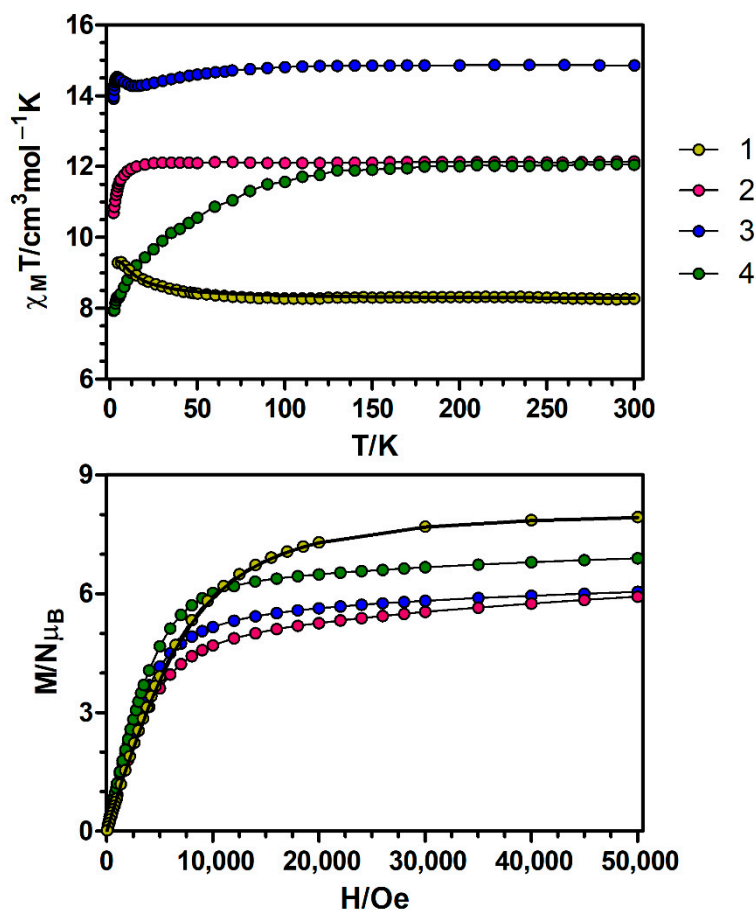


Figure 3. Top: Temperature dependence of the $\chi_M T$ product at 1000 Oe for complexes 1–4. Bottom: M versus H plots for complexes 1–4 at 2 K. The black solid lines show the best fits for complex 1. The rest of the lines are a guide to the eye.

To support the experimental value of J_{CuGd} , DFT calculations were carried out on the X-ray structure as found in the solid state. The calculated J_{CuGd} parameter of $+2.51 \text{ cm}^{-1}$ matches very well in sign and magnitude with the experimental one. Previous theoretical studies carried out on dinuclear $\text{Cu}-(\mu\text{-O})_2\text{-Gd}$ complexes indicate that ferromagnetic interactions between Cu^{II} and Gd^{III} ions increase with the planarity of the $\text{Cu}-(\mu\text{-O})_2\text{-Gd}$ bridging fragment and with the increase of the Cu-O-Gd angle [19–21]. Therefore, the weak ferromagnetic interactions found in this complex are not unexpected if we consider the mean Cu-O-Gd angle of 99.60° and the dihedral β angle of 25.07° .

The $\chi_M T$ values of 12.14 , 14.87 and $12.06 \text{ cm}^3 \cdot \text{K} \cdot \text{mol}^{-1}$ respectively for complexes 2–4 at 300 K are compatible with the expected values or pairs of magnetically isolated Cu^{II} and Ln^{III} ions (Table S11). On lowering the temperature, the $\chi_M T$ product of the $\text{Cu}^{\text{II}}\text{Dy}^{\text{III}}$ dimer (3) decreases gradually to reach a minimum value of $14.28 \text{ cm}^3 \cdot \text{K} \cdot \text{mol}^{-1}$ at 14 K and then increases until $14.53 \text{ cm}^3 \cdot \text{K} \cdot \text{mol}^{-1}$ at 4.0 K. Below this temperature, there is a small decrease to reach a value of $13.99 \text{ cm}^3 \cdot \text{K} \cdot \text{mol}^{-1}$ at 2.0 K. The magnetic behaviour at low temperatures of this complex is the result of two competing interactions: (1) ferromagnetic exchange interactions between the Cu^{II} and Dy^{III} ions, which lead to an increase in $\chi_M T$ and (2) crystal field splitting of the Dy^{III} ions, responsible for the decrease in $\chi_M T$. The fact that $\chi_M T$ increases at low temperatures suggests that ferromagnetic interactions prevail over the

effect of the crystal field splitting in this complex. On the other hand, the $\chi_M T$ products of complexes **2** and **4** remain constant on cooling until 25 and 130 K, respectively, and then drop abruptly to reach respectively values of 10.70 and 7.93 $\text{cm}^3 \cdot \text{K} \cdot \text{mol}^{-1}$ at 2 K. The decrease of $\chi_M T$ in the low temperature regime for **2** and **4** seems to indicate that in these compounds the effect of ferromagnetic exchange interactions is not as pronounced as in **3**. The nature of the exchange interaction between Cu^{II} and lanthanide ions displaying spin-orbit coupling (SOC) can be known by the empirical approach developed by Costes et al. [22], which consists on representing the temperature dependence of the difference $\Delta\chi_M T = \chi_M T_{(\text{CuLn})} - \chi_M T_{(\text{ZnLn})} = \chi_M T_{(\text{Cu})} + J_{(\text{CuGd})}$, where the contribution of the crystal-field effects of the Ln^{III} ions is removed from the $\chi_M T_{(\text{CuLn})}$ data. The results obtained by this procedure using the magnetic data of the Zn^{II} -based analogues [16] reveal that the $\Delta\chi_M T$ differences show an increase at low temperatures (Figure S2), thus suggesting the occurrence of ferromagnetic interaction between Cu^{II} and Ln^{III} ions in complexes **2–4**.

Upon increasing the applied external magnetic field, the magnetization of complexes **2–4** shows a relatively rapid increase at low magnetic fields and a rapid saturation that is almost complete above 4 T, reaching values of 5.92, 6.04 and 6.89 $\text{N}\mu_B$ at 5 T respectively. These values are quite far from the expected saturation values (10 $\text{N}\mu_B$ for complexes **2** and **4** and 11 $\text{N}\mu_B$ for complex **3**), which suggests the presence of a significant magnetic anisotropy due to the crystal field effects and/or most likely the presence of low-lying excited states that are partially (thermally and field-induced) populated.

Continuing with the $\text{Ni}(\text{II})$ -based complexes, the temperature dependence of $\chi_M T$ for complexes **5–10** (χ_M is the molar magnetic susceptibility per $\text{Ni}^{\text{II}}\text{Ln}^{\text{III}}$ unit) were measured in an applied field of 0.1 T and are displayed in Figure 4. Let us start with the simplest cases, the Ni–Gd (**6**) and Ni–Y (**10**) dimers. At room temperature the $\chi_M T$ value of complex **6** is 9.38 $\text{cm}^3 \cdot \text{K} \cdot \text{mol}^{-1}$, which is slightly high but still in good agreement with the expected value for a couple of non-interacting Ni^{II} ($S = 1$) and Gd^{III} ($S = 7/2$) ions (8.875 $\text{cm}^3 \cdot \text{K} \cdot \text{mol}^{-1}$). The $\chi_M T$ value increases very slowly with decreasing temperature until 70 K and then in a more abrupt way to reach a maximum value of 10.82 $\text{cm}^3 \cdot \text{K} \cdot \text{mol}^{-1}$ at 3.3 K. Below the temperature of the maximum, there is a small decrease to reach a value of 10.67 $\text{cm}^3 \cdot \text{K} \cdot \text{mol}^{-1}$ at 2.0 K (Figure S3). The increase in $\chi_M T$ indicates the existence of intramolecular ferromagnetic interactions between Ni^{II} and Gd^{III} ions, whereas the decrease at low temperatures is more likely due to the zero field splitting effects (ZFS) of the ground state and/or intermolecular antiferromagnetic (AF) interactions. The field dependence of the magnetization at 2 K for **6** (Figure 4) reveals a relatively rapid increase at low fields to reach a clear saturation that is almost complete at 3 T, reaching a value of 9.01 $\text{N}\mu_B$ at 5 T. This value is in good agreement with the expected value for the fundamental state $S_T = 9/2$ with $g = 2$ (9 $\text{N}\mu_B$).

On the other hand, the $\chi_M T$ value of the NiY complex (**10**) at room temperature is 1.23 $\text{cm}^3 \cdot \text{K} \cdot \text{mol}^{-1}$, which is compatible with the calculated value of 1 $\text{cm}^3 \cdot \text{K} \cdot \text{mol}^{-1}$ for independent Ni^{II} ions. On cooling, the $\chi_M T$ value remains almost constant until 18 K and then drops abruptly to reach a value of 0.957 $\text{cm}^3 \cdot \text{K} \cdot \text{mol}^{-1}$ at 5 K, which is due to the zero field splitting (ZFS) of Ni^{II} ion. The magnetization of complex **10** shows a gradual increase with the applied external field reaching a value of 1.57 $\text{N}\mu_B$ at 5 T, which is lower than the expected from the Brillouin function for an $S = 1$ ground state (2 $\text{N}\mu_B$). This behaviour is due to the strong zero field splitting of the Ni^{II} ion, which leads to the split of the $S = 1$ ground state into two $M_s = 0, \pm 1$ components, preventing the magnetization from reaching the expected value.

The magnetic behaviour of complex **6** has been modelled using the following Hamiltonian formula:

$$H = -J S_{\text{Ni}} S_{\text{Gd}} + D_{\text{Ni}} S_{\text{Ni}}^2 + g_e \mu_B S H \quad (2)$$

where J is the coupling constant between the Ni^{II} and Gd^{III} ions, D_{Ni} is the ZFS parameter for Ni^{II} ion, g_e is the average g factor, μ_B is the Bohr magneton and H is the magnetic field. The best-fit parameters to the experimental susceptibility and magnetization data using the PHI program [18] afforded the following set of parameters: $J = +0.71 \text{ cm}^{-1}$, $g = 2.06$ and $D = 6.73 \text{ cm}^{-1}$ with $R = 9.76 \times 10^{-6}$. The value of the D_{Ni} parameter for the NiY complex

extracted from the simultaneous fit of the susceptibility and magnetization data ($D_{\text{Ni}} = 6.61 \text{ cm}^{-1}$, $g = 2.23$ and $R = 1.24 \times 10^{-4}$, Figure 4) supports the magnitude of the D_{Ni} obtained for the Gd^{III} -based analogue. Regarding J , it should be noted that when D_{Ni} was fixed to zero and a term accounting for the intermolecular interactions was introduced in the Hamiltonian by means of the molecular field approximation, $-zJ' < S_z > S_z$, the fitting parameters did not significantly change: $J = +0.81 \text{ cm}^{-1}$, $g = 2.06$ and $zJ' = -0.008 \text{ cm}^{-1}$ with $R = 3.82 \times 10^{-5}$.

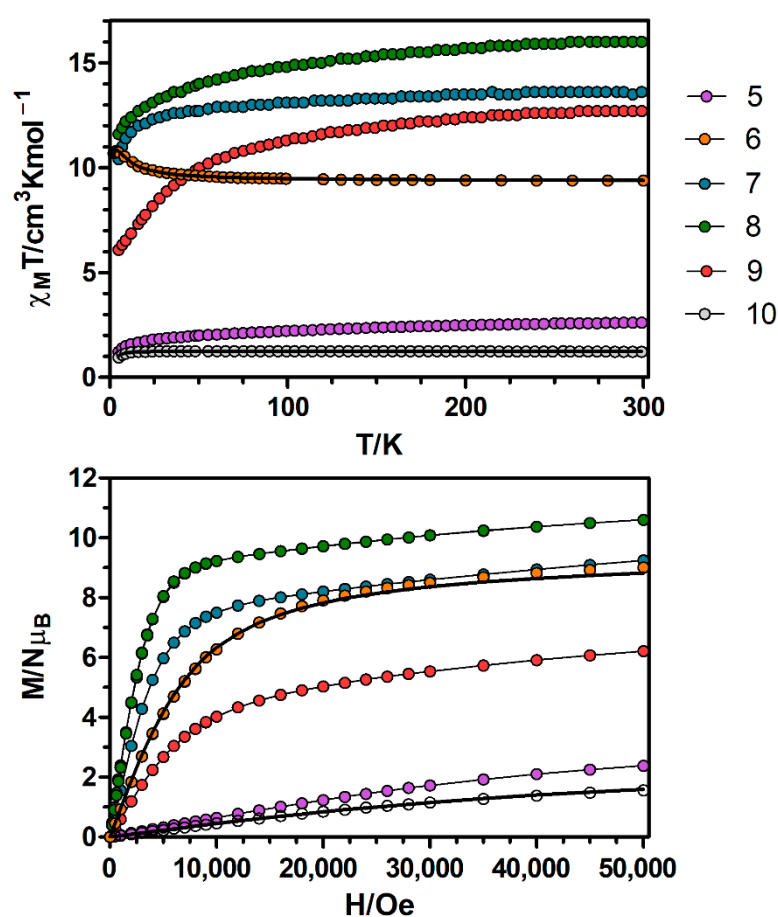


Figure 4. Top: Temperature dependence of the $\chi_M T$ product at 1000 Oe for complexes 5–10. Bottom: M versus H plots for complexes 5–10 at 2 K. Black solid lines show the best fits for complexes 6 and 10. The rest of the lines are a guide to the eye.

In order to support the experimental J value found for complex 6, DFT calculations were carried out on the X-ray structure using the broken-symmetry approach. The calculated J_{NiGd} parameter of $+0.87 \text{ cm}^{-1}$ agrees very well in sign and magnitude with the experimental parameters. The obtained experimental value is at the lower end of the experimental range found for alkoxo and phenoxo bridged Ni_xGd ($x = 1, 2, 3$) complexes with ferromagnetic interactions [23,24], which is due to the relatively small Ni–O–Gd angle (100.05°) and large Ni–($\mu\text{-O}$) $_2$ –Gd dihedral angle (28.29°) found in this complex. In fact, it has been seen from experimental results and DFT calculations that in diphenoxido bridged dinuclear NiGd complexes the ferromagnetic coupling increases when increasing the planarity of the Ni–($\mu\text{-O}$) $_2$ –Gd bridging fragment and the Ni–O–Gd bridging angle [23,24]. In addition, the effect of a third non-phenoxido bridge in the magnetic exchange coupling was also studied in the structurally similar complex $[\text{Ni}(\mu\text{-L}^1)(\mu\text{-OAc})\text{Gd}(\text{NO}_3)_2]$ ($\text{H}_2\text{L}^1 = N,N',N''\text{-trimethyl-}N,N''\text{-bis(2-hydroxy-3-methoxy-5-methylbenzyl)diethylenetriamine}$), which was done by substituting the *syn-syn* acetate bridging group by two non-bridging water molecules [23]. The results of the calculations showed an increase of 0.45 cm^{-1} in

J_{NiGd} , indicating that the third bridge has a significant role in decreasing the magnetic exchange coupling in this type of compounds. Therefore, in view of the above considerations the weak ferromagnetic interaction between the Ni^{II} and Gd^{III} ions is not unexpected.

With respect to complexes **5** and **7–9**, at room temperature the $\chi_{\text{M}}T$ values are in general close but slightly higher than the expected values for pairs of magnetically isolated Ni^{II} and Ln^{III} ions (Table S11). On lowering the temperature, the $\chi_{\text{M}}T$ values decrease gradually until ~50 K and then drop abruptly to reach a minimum value of 1.23 cm³·K·mol⁻¹ for complex **5** and values that at 5 K are in the 6.04–11.6 cm³·K·mol⁻¹ range for complexes **7–9**. As in the case of complexes **1–4**, this behaviour is due to the depopulation of M_{J} sublevels of the Ln^{III} ions. The empirical approach developed by Costes et al. to know the nature of the interactions between the Ni^{II} and Ln^{III} ions cannot be used for these complexes, because they are not isostructural to the Zn^{II}Ln^{III} complexes reported previously.

The magnetization of complexes **7–9** (Figure 4) show relatively rapid increase at low fields, in accordance with the ferromagnetic interaction between Ni^{II} and Ln^{III} ions and a lineal increase from 1 T without reaching a clear saturation at 5 T. The magnetization values at 5 T for complexes **7** and **8** (Table S11) are close to the expected saturation magnetization values for Ln^{III} ions with strong easy-axis anisotropy that behave as Ising type ions and that are ferromagnetically coupled to Ni^{II} ions. The M value for **9** at 5 T, however, is considerably lower than the expected saturation value, which could indicate that the latter compound shows weaker axial anisotropy than complexes **7** and **8**. Moreover, the magnetization of complex **5** shows a gradual increase with the applied magnetic field, reaching a value of 2.4 $N\mu_{\text{B}}$ at 5 T.

The temperature dependence of $\chi_{\text{M}}T$ for complexes **11–15** (χ_{M} is the molar susceptibility per Co^{II}Ln^{III} unit) were measured in an applied field of 0.1 T and are displayed in Figure 5. The $\chi_{\text{M}}T$ value for the CoY complex **15** at room temperature (2.72 cm³·K·mol⁻¹) is significantly larger than the spin-only value for a high-spin Co^{II} ion ($S = 3/2$, 1.875 cm³·K·mol⁻¹ with $g = 2$), which is indicative of the unquenched orbital contribution of the Co^{II} ion in distorted octahedral geometry. Upon cooling, $\chi_{\text{M}}T$ remains practically constant in the high temperature range and it decreases sharply below 120 K, reaching a value of 1.82 cm³·K·mol⁻¹ at 4.5 K (Figure S4). As the molecules are well isolated in the crystal field, this decrease is most likely due to SOC effects rather than intermolecular AF interactions. The susceptibility data was fitted to Equation 3 with the PHI program [18], obtaining the following set of parameters: $\lambda = -104.0 \text{ cm}^{-1}$, $\alpha = 1.216$, $\Delta = |355.3| \text{ cm}^{-1}$ and $\delta = |89.35| \text{ cm}^{-1}$ with $R = 3.51 \times 10^{-6}$. The fit of the experimental data to the theoretical equation shows that the sign of Δ cannot be unambiguously determined from the susceptibility data, as the agreement factor (R) for positive and negative values are, in general, close. The fitting parameters are in good accordance with previously reported values for distorted octahedral Co^{II} complexes [25–27].

$$H = -\alpha\lambda LS + \Delta \left[L_z^2 - L(L+1)/3 \right] + \delta \left(L_x^2 - L_y^2 \right) + \beta H(-\alpha L + g_e S) \quad (3)$$

Regarding the magnetization plot of complex **15**, at an applied field of 5 T the magnetization is not fully saturated, reaching a value of 2.6 $N\mu_{\text{B}}$ (Figure 5 and Figure S4). This value is lower than the expected saturation value of 3 $N\mu_{\text{B}}$, which is due to anisotropy. The M vs. H/T plots obtained between 2 and 7 K at applied magnetic fields ranging from 0.1 to 9 T (Figure S5) are not superimposed on a single master curve, indicating that complex **15** shows a significant magnetic anisotropy. In order to quantify this anisotropy, the magnetic susceptibility data were fitted to Equation 4 using the PHI program [18], obtaining the following set of parameters: $D = |35.5| \text{ cm}^{-1}$ and $g = 2.43$ with $R = 1.2 \times 10^{-4}$.

$$H = D \left[S_z^2 - S(S+1)/3 \right] + g_e \mu_{\text{B}} S H \quad (4)$$

where S is the spin ground state, D is the axial magnetic anisotropy, g_e is the average g factor, μ_{B} is the Bohr magneton and H is the magnetic field. The sign of D cannot be unambiguously determined from the susceptibility data either in this case.

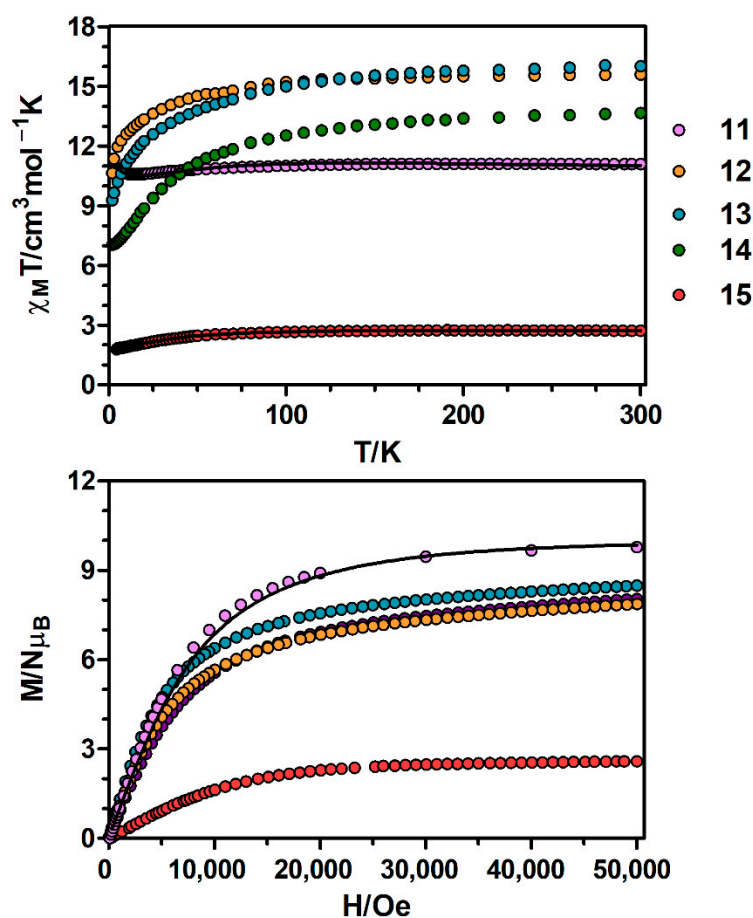


Figure 5. Top: Temperature dependence of the $\chi_M T$ product at 1000 Oe for complexes **11**–**15**. Bottom: M versus H plots for complexes **11**–**15** at 2 K. Black solid lines show the best fits for complexes **11** and **15**.

Continuing with the CoGd complex **11**, at room temperature the $\chi_M T$ value of $11.09 \text{ cm}^3 \cdot \text{K} \cdot \text{mol}^{-1}$ is slightly larger than the expected value for two non-interacting Co^{II} ($S = 3/2$) and Gd^{III} ($S = 7/2$) ions ($9.750 \text{ cm}^3 \cdot \text{K} \cdot \text{mol}^{-1}$ with $g = 2.0$), which may be due to the orbital contribution of Co^{II} ions. On cooling, the $\chi_M T$ product stays constant until 140 K, then starts decreasing to reach a minimum value of $10.58 \text{ cm}^3 \cdot \text{K} \cdot \text{mol}^{-1}$ at 15 K and ends up increasing until $10.90 \text{ cm}^3 \cdot \text{K} \cdot \text{mol}^{-1}$ at 4.5 K (Figure 5 and Figure S6). The observed decrease of $\chi_M T$ is due to the thermal depopulation of the spin-orbit coupling levels arising from the $^4T_{1g}$ ground term of Co^{II} ions, whereas the increase at low temperature indicates a ferromagnetic interaction between Co^{II} and Gd^{III} ions.

The magnetic behaviour of complex **11** was analysed by considering both effects and a purely octahedral Co^{II} coordination environment, as included in the following Hamiltonian formula:

$$H = \alpha \lambda LS - JS_{\text{Co}}S_{\text{Gd}} \quad (5)$$

The fit of the experimental susceptibility data using the above equation led to the following parameters: $\lambda = -111.2 \text{ cm}^{-1}$, $\alpha = 0.88$, $J = +0.26 \text{ cm}^{-1}$ and $g = 2.06$ (considered to be the same for both ions) with $R = 2.52 \times 10^{-5}$. The observed coupling constant is lower than that found for the similar di- μ -phenoxo/*syn-syn* acetate triply bridged compound $[\text{Co}(\mu\text{-L}^1)(\mu\text{-OAc})\text{Gd}(\text{NO}_3)_2]$ ($J = +0.7 \text{ cm}^{-1}$) [28,29], and to those found for planar di- μ -phenoxo-bridged $\text{Co}^{\text{II}}\text{Gd}^{\text{III}}$ complexes containing a compartmental ligand ($J \sim 1 \text{ cm}^{-1}$) [30,31]. Following the considerations made for $\text{Cu}^{\text{II}}\text{Gd}^{\text{III}}$ and $\text{Ni}^{\text{II}}\text{Gd}^{\text{III}}$ complexes, the observed low value of J is not unexpected if we take into account that **11** has the highest hinge angle.

The magnetization isotherm of **11** at 2 K (Figure 5 and Figure S6) shows a relatively rapid increase at low field, in agreement with a high spin ground state and a rapid saturation of the magnetization at higher fields to reach a value of $9.79 N\mu_B$ at 5 T, which is close to the expected saturation value for a couple of Co^{II} and Gd^{III} ions with $g = 2.0$ ($10 N\mu_B$). The experimental magnetization data falls slightly above the Brillouin curve for a pair of non-interacting Co^{II} ($S = 3/2$) and Gd^{III} ($S = 7/2$) ions with $g = 2.06$, thus confirming the existence of very moderate ferromagnetic interaction between the metal ions.

Regarding **12–14**, the $\chi_M T$ values at room temperature are higher than those calculated for independent Co^{II} ($S = 3/2$, $g = 2$) and Ln^{III} ions in the free-ion approximation (Figure 5, Table S11), which is mainly due to the orbital contribution of the Co^{II} ion. The $\chi_M T$ products remain constant with decreasing temperature until 100 K and then decrease abruptly reaching the values listed in Table S11 at 2 K. This behaviour is due to both thermal depopulation of the levels that arise from spin-orbit coupling in the Co^{II} ion and the thermal depopulation of the M_j sublevels of the Ln^{III} ion.

Finally, as shown in Figure 5, upon increasing the applied external magnetic field, the magnetization of complexes **12–14** are increased to 7.87, 8.49 and 8.05 $N\mu_B$ at 5 T, respectively, but do not reach the expected saturation values (Table S11) for a couple of Co^{II} and Ln^{III} ions. The observed behaviour is due to the anisotropy of the Co^{II} and Ln^{III} ions.

3.2. Dynamic Magnetic Properties

Dynamic alternating current (*ac*) magnetic susceptibility measurements as a function of the temperature at different frequencies were performed on the most promising complexes. However, under zero-external field none of them showed frequency dependency of the in-phase (χ_M') and out-of-phase signals (χ_M''), which could be due to fast resonant zero-field quantum tunnelling of the magnetization (QTM) through degenerate energy levels. When the *ac* measurements were performed in the presence of a small external direct current (*dc*) field of 1000 Oe, complexes **8** ($\text{Ni}^{\text{II}}\text{Dy}^{\text{III}}$), **9** ($\text{Ni}^{\text{II}}\text{Er}^{\text{III}}$) and **13** ($\text{Co}^{\text{II}}\text{Dy}^{\text{III}}$) showed a weak frequency dependency, but with the maxima of χ_M'' appearing below the instrument detection limit (Figures S7 and S8). Thus, the energy barrier (U_{eff}) and relaxation time (τ_0) cannot be obtained via the conventional Arrhenius method. However, if we assume that there is only one relaxation process, the Debye model (Equation (6)) could provide a rough estimate of U_{eff} and τ_0 values [32],

$$\ln \frac{\chi_M''}{\chi_M'} = \ln(2\pi\nu\tau_0) + \frac{E_a}{k_B T} \quad (6)$$

yielding U_{eff} values of 7.76, 11.91 and 12.30 K and relaxation times (τ_0) of 5.78×10^{-7} , 5.12×10^{-8} and 7.76×10^{-9} s for complexes **8**, **9** and **13**, respectively (Figure S8). Thus, all these results highlight that the simple mixing of *3d* and *4f* ions does not always lead to the desired behaviour. The worsening of the properties compared to the $\text{Zn}^{\text{II}}\text{Ln}^{\text{III}}$ analogues [16] has been ascribed to the weak exchange interactions between the *3d* and *4f* ions, which generate multiple low-lying excited states separated by small energies. In addition, due to the weak exchange interactions, the *3d* metal ions can create random transversal fields for the lanthanide ions, thus favouring the quantum tunnelling of the magnetization [33–39].

Finally, $\text{Co}^{\text{II}}\text{Y}^{\text{III}}$ complex **15** displays slow relaxation of the magnetization with maxima below ~6 K after the application of an external field of 1000 Oe (Figure 6). Note that this field was chosen because it induces the slowest relaxation rate, which does not significantly vary until fields as high as 3500 Oe (Figure S9). The Cole–Cole diagrams obtained under this field in the temperature range 2.0–6.4 K exhibit semicircular shapes, with α values in the 0.27–0.05 range, suggesting multiple relaxation processes (Figure S10). The temperature dependence of the magnetic relaxation times were used to construct an Arrhenius plot, which led to an effective energy barrier for the reversal of the magnetization of 15.68 K with $\tau_0 = 1.73 \times 10^{-6}$ s. The obtained U_{eff} is much lower than the expected value from the energy gap between the $M_s = \pm 1/2$ and $M_s = \pm 3/2$ levels from *dc* measurements (energy gap = $2D = 71 \text{ cm}^{-1} = 102 \text{ K}$ assuming $E = 0$), but in good agreement with those found

for other monometallic Co^{II} SMMs exhibiting $D > 0$ and field induced slow relaxation of the magnetization through a Raman mechanism, which show apparent U_{eff} values of $\sim 20 \text{ cm}^{-1}$ [25].

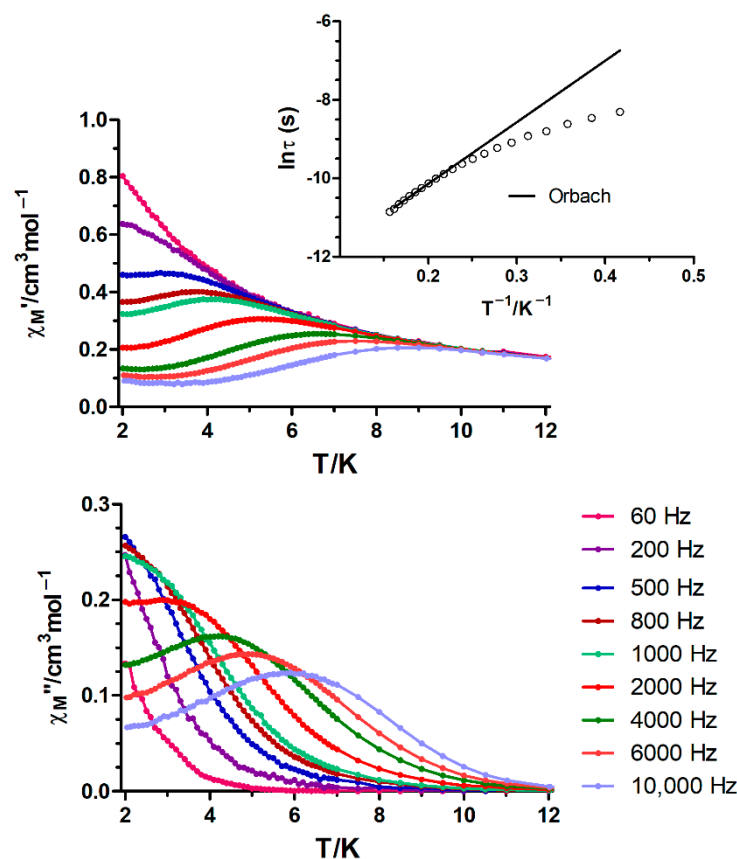


Figure 6. Temperature dependence of in-phase χ_M' and out-of phase χ_M'' components of the alternating current ac susceptibility for complex **15** under an applied field of 1000 Oe. Inset: Arrhenius plot for the temperature dependence of the relaxation times of **15** (black line).

3.3. Magneto-Thermal Properties

Magnetic isotropy and high ground spin-state are two factors that favour the observation of a large magneto-caloric effect (MCE) [15,40–44]. Moreover, if the magnetic exchange interaction between the metal ions is weak, a large MCE could be attained [15,40–44]. Thus, the isotropic nature of the Cu^{II} and Gd^{III} ions and the weak ferromagnetic exchange interactions, as well as the relatively large metal/ligand mass ratio (which limits the amount of passive, non-magnetic elements) makes compound **1** a good candidate to display large MCE. For comparative purposes, the magnetic entropy changes ($-\Delta S_m$) that characterize the MCE have also been calculated for the $\text{Ni}^{\text{II}}\text{Gd}^{\text{III}}$ complex (**6**), as Ni^{II} ions generally exhibit weak second-order spin-orbit anisotropy (ZFS zero-field splitting). However, MCE has not been measured for the $\text{Co}^{\text{II}}\text{Gd}^{\text{III}}$ compound (**11**), because, as is well known, octahedral Co^{II} ions exhibit a large first-order magnetic anisotropy that significantly reduces the MCE effect.

The fitting of the experimental isothermal magnetization data (Figure 7 and Figure S12) to the Maxwell relation (Equation (7), B_i and B_f are the initial and final applied magnetic fields, respectively) leads to maximum $-\Delta S_m$ values that appear in Table 1.

$$\Delta S_m = (T, \Delta B) = \int_{B_i}^{B_f} \left[\frac{\partial M(T, B)}{\partial T} \right]_B dB \quad (7)$$

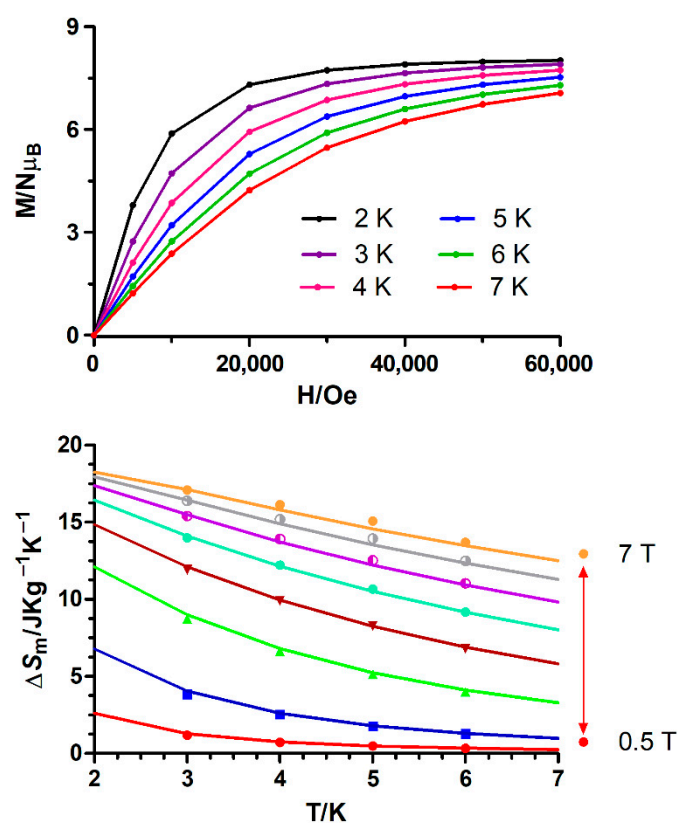


Figure 7. Top: Field dependence of the magnetization at different temperatures for **1**. The solid lines are a guide to the eye. Bottom: Magnetic entropy changes extracted from the experimental magnetization data for **1**. The solid lines represent the values calculated from the magnetic parameters (J , g and zJ) indicated in the text.

Table 1. Maximum magnetic entropy change values ($-\Delta S_m$) for complexes **1** and **6** and for $[\text{Mn}(\text{CH}_3\text{OH})(\mu\text{-L}^1)\text{Gd}(\text{NO}_3)_3]$ at 7 T.

Complex	S_T	J (cm^{-1})	$-\Delta S_m$ Max ($\text{J}\cdot\text{kg}^{-1}\cdot\text{K}^{-1}$)	T/K
1	4	+2.3	17.1	3
6	9/2	+0.7	17.4	3
$[\text{Mn}(\text{CH}_3\text{OH})(\mu\text{-L}^1)\text{Gd}(\text{NO}_3)_3]^a$	6	+0.99	23.5	2.7

^a $\text{H}_2\text{L}^1 = N,N',N''\text{-trimethyl-}N,N''\text{-bis(2-hydroxy-3-methoxy-5-methylbenzyl)-diethylenetriamine}$ [45].

The integration results for **1** and **6** display a gradual increase of $-\Delta S_m$ with decreasing temperature from 6 K to 2 K (Figure 7 and Figure S12) and increasing applied magnetic field. The simulation of the temperature and field dependence of $-\Delta S_m$ for **1** (solid lines in Figure 7), using the magnetic parameters (g , J and zJ) extracted from the fitting of the magnetization and susceptibility data, show that the $-\Delta S_m$ values are almost coincident with those extracted from the integration of the field dependence of the magnetization (Figure 7) at different temperatures, thus supporting the $-\Delta S_m$ values extracted from experimental magnetization data. The $-\Delta S_m$ reaches a maximum value of $17.09 \text{ J}\cdot\text{kg}^{-1}\cdot\text{K}^{-1}$ for $\Delta H = 7 \text{ T}$ at 3.0 K, which is smaller than the full magnetic entropy content per mole of the $\text{Cu}^{\text{II}}\text{Gd}^{\text{III}}$ complex ($23.67 \text{ J}\cdot\text{kg}^{-1}\cdot\text{K}^{-1}$, calculated by means of the expression $\text{Rln}(2S_{\text{Gd}} + 1) + \text{Rln}(2S_{\text{Cu}} + 1) = 2.77 \text{ R}$). Even though the simulated MCE value at 2 K and 7 T ($18.26 \text{ J}\cdot\text{kg}^{-1}\cdot\text{K}^{-1}$) is lower than that calculated for the full magnetic entropy content for **1**, it is close to the value expected for a ferromagnetically coupled $\text{Cu}^{\text{II}}\text{Gd}^{\text{III}}$ dimer ($2.19 \text{ R} = 18.82 \text{ J}\cdot\text{kg}^{-1}\cdot\text{K}^{-1}$). Compared to other $\{\text{CuGd}\}_n$ complexes, the $-\Delta S_m$ (simulated at 2K)/ $-\Delta S_m$ (full entropy content) ratio of 0.77 obtained for **1** is slightly lower than the 0.83 ratio observed for the Cu_6Gd_6 com-

plex $[\{(HL^2)(L^2)(DMF)Cu^{II}Gd^{III}(DMF)(H_2O)\}_6] \cdot 6DMF$ ($DMF = N,N$ -dimethylformamide; $H_3L^2 =$ Schiff base obtained from the condensation of 3-formylsalicylic acid with hydroxylamine) [46]. This fact can be because $[\{(HL^2)(L^2)(DMF)Cu^{II}Gd^{III}(DMF)(H_2O)\}_6] \cdot 6DMF$ exhibits weaker ferromagnetic interactions ($J = +1.01 \text{ cm}^{-1}$) than **1**, which favours the spin polarization at relatively low magnetic fields (the stronger the ferromagnetic interaction, the smaller the MCE). However, $[Gd^{III}_2Cu^{II}_2(OH)_2(NO_3)_{2.5}(OAc)_{3.5}(L^3)_2]_n$ ($L^3 = 2$ -pyridinylmethanol) [47] displays a ratio of 0.56 due to strong CuGd magnetic interactions, with calculated absolute values in the $3.2\text{--}4.2 \text{ cm}^{-1}$ range. It is worth noting that, as expected, the maximum $-\Delta S_m$ value observed for **1** with a Gd/Cu = 1 is generally larger than those found for other less magnetic dense complexes with Gd/Cu ratios lower than 1.

For the $Ni^{II}Gd^{III}$ complex (**6**) the maximum value of $-\Delta S_m$ is of $17.38 \text{ J} \cdot \text{kg}^{-1} \cdot \text{K}^{-1}$ at $T = 3 \text{ K}$ and an applied field change $\Delta H = 7 \text{ T}$ (Figure S12, inset). This value is also smaller than the full magnetic entropy content per mole, which is of $3.18 \text{ R} = 28.41 \text{ J} \cdot \text{kg}^{-1} \cdot \text{K}^{-1}$. However, this value is close to the expected value for a ferromagnetically coupled $Ni^{II}Gd^{III}$ complex ($2.30 \text{ R} = 18.55 \text{ J} \cdot \text{kg}^{-1} \cdot \text{K}^{-1}$). The temperature dependence of the $-\Delta S_m$ values at different applied magnetic fields (Figure S12, inset) can be reproduced reasonably well using the magnetic parameters (J , g and D) extracted from the simultaneous fitting of the magnetic and susceptibility data, thus underpinning the $-\Delta S_m$ values extracted from the field and temperature dependence of the magnetization. Compared to other $(NiGd)_n$ systems, such as Ni_6Gd_6 [48] and Ni_2Gd_2 [49] with $-\Delta S_m$ values of 26.5 and $34.4 \text{ J} \cdot \text{kg}^{-1} \cdot \text{K}^{-1}$, respectively, compound **6** exhibits a lower $-\Delta S_m$ value and a smaller $-\Delta S_m$ (simulated at 2K)/ $-\Delta S_m$ (full entropy content) ratio (0.70 and 0.91 for the two former compounds and 0.61 for compound **6**). This latter fact could be due to both a larger J value and a larger magnetic anisotropy for **6** compared to the other $(NiGd)_n$ systems. Even though complex **1** has lower S_T and higher J values than **6**, both complexes exhibit similar MCE. This result shows clearly the relatively stronger impact of the anisotropy of the Ni^{II} ion on the MCE. It is worth mentioning that the closely structurally related $Mn^{II}Gd^{III}$ dinuclear complex, previously reported by one of us [45], displays the largest $-\Delta S_m$ value in this series. This fact is not surprising taking into account that in this compound both paramagnetic ions are magnetically isotropic, the S_T is the largest in the series and the J value is rather small.

4. Materials and Methods

4.1. General Procedures

All analytical reagents were purchased from commercial sources and used without further purification. All syntheses were performed under ambient laboratory atmosphere. The H_2L ligand was prepared according to a previously described procedure [50].

4.2. Preparation of Complexes

$[Cu(\mu-L)(\mu-OAc)Ln(NO_3)_2] \cdot CH_3CN \cdot H_2O$ ($Ln^{III} = Gd$ (**1**), Tb (**2**), Dy (**3**), Er (**4**)). A general procedure was used for the preparation of these complexes: to a solution of 25.0 mg (0.125 mmol) of $Cu(OAc)_2 \cdot H_2O$ in 5 mL of acetonitrile/methanol (80:20) mixture were added with continuous stirring 64.3 mg (0.125 mmol) of H_2L and 0.125 mmol of the corresponding $Ln(NO_3)_3 \cdot nH_2O$. The resulting solution was filtered and allowed to stand at room temperature. After several days, well-formed prismatic dark green crystals of compounds **1–4** were obtained in yields in the range 35–41% (Supporting Information, Table S1), which were filtered, washed with acetonitrile and air-dried.

$[Ni(CH_3CN)(\mu-L)(\mu-OAc)Ln(NO_3)_2] \cdot CH_3CN$ ($Ln^{III} = Nd$ (**5**), Gd (**6**), Tb (**7**), Dy (**8**), Er (**9**), Y (**10**)). These compounds were prepared with yields in the range 45–57% (Supporting Information, Table S1) following the procedure for **1–4**, but using $Ni(OAc)_2 \cdot 4H_2O$ (31.1 mg, 0.125 mmol) instead of $Cu(OAc)_2 \cdot H_2O$.

$[Co(CH_3CN)(\mu-L)(\mu-OAc)Ln(NO_3)_2] \cdot CH_3CN$ ($Ln^{III} = Gd$ (**11**), Tb (**12**), Dy (**13**), Er (**14**), Y (**15**)). These compounds were prepared as orange crystals following the same procedure as for **1–4**, except that $Co(OAc)_2 \cdot 4H_2O$ (31.1 mg, 0.125 mmol) was used as source of metal. Yields: 39–54%.

The purity of the complexes was checked by elemental analysis (Supporting Information, Table S1).

4.3. Physical Measurements

Elemental (C, H, and N) analyses were performed on a Leco CHNS-932 microanalyzer (Elemental Microanalysis Ltd., Devon, UK). Infrared spectra were recorded in the region 400–4000 cm^{-1} on a Nicolet 6700 FTIR (Fourier transform infrared) spectrophotometer (Thermo Fisher Scientific, TX, USA) with samples as KBr disks. Variable temperature magnetic susceptibility measurements and magnetization measurements at 2 K on polycrystalline samples were measured in several devices: a PPMS (physical property measurement system)—Quantum Design Model 6000 magnetometer, a Quantum Design SQUID MPMS XL-5 device and a Quantum Design SQUID MPMS-7T device (Quantum Design, San Diego, CA, USA). Alternating current magnetic measurements in a 3.5 G *ac* field oscillating at 60–10,000 Hz were performed on a PPMS—Quantum Design Model 6000 magnetometer.

4.4. Single-Crystal Structure Determination

Single crystals of suitable dimensions were used for data collection. Intensity data for compounds **1**, **6**, **8**, **10**, **12** and **13** were collected at 100 (2) K on an Agilent Technologies SuperNova diffractometer (mirror-monochromated Mo $K\alpha$ radiation, $\lambda = 0.71073 \text{ \AA}$) equipped with an Eos CCD detector. In the case of compounds **2–4**, **9** and **14**, data collection was also carried out at 100 (2) K, but the Supernova diffractometer was equipped with Cu $K\alpha$ radiation ($\lambda = 1.54184 \text{ \AA}$) and an Atlas CCD detector. In all cases, data frames were processed (unit cell determination, intensity data integration, correction for Lorentz and polarization effects, and analytical absorption correction) using the CrysAlis software package [51].

Diffraction intensities of compounds **5** and **7** were collected on a Bruker SMART X2S benchtop diffractometer, with doubly curved silicon crystal monochromated Mo $K\alpha$ ($\lambda = 0.71073 \text{ \AA}$) radiation and Breeze CCD detector at 200 (2) K. Finally, the collection of the diffraction intensities for **11** and **15** were carried out with a Bruker 8 Venture with a photon detector equipped with graphite monochromated Mo $K\alpha$ ($\lambda = 0.71073 \text{ \AA}$) radiation. For data reduction, the Bruker Saint program was used [52]. The data were corrected for Lorentz and polarization effects and an empirical absorption correction (SADABS) was applied [53].

The structures were solved by direct methods and refined by full-matrix least-squares with SHELX-2014 [54]. Anisotropic temperature factors were assigned to all atoms except for the hydrogen atoms, which are riding their parent atoms with an isotropic temperature factor arbitrarily chosen as 1.2 times that of the respective parent. The crystal data for **1–15** along with some refinement details are summarized in Supporting Information Tables S2–S4. Selected bond lengths and angles are given in Supporting Information Tables S5 and S6. Cambridge Crystallographic Data Centre (CCDC) reference numbers for the structures are 2052561–2052575.

4.5. Computational Details

Theoretical coupling constants were calculated using the broken symmetry approach proposed by Noodleman et al. [55–57]. All theoretical calculations were carried out at the density functional theory (DFT) level using the hybrid density functional B3LYP (Becke, 3-parameter, Lee–Yang–Parr) [58–61] as implemented in the Gaussian 09 program [62]. The triple- ζ quality 6–311G* basis set was used for all electrons in non-metal atoms, while the CREMBEL pseudopotential was used for core electrons of metal atoms [63,64]. Calculations were performed on complexes **1** and **6** derived from experimental crystallographic geometries. The approach used to determine the exchange coupling constants for polynuclear complexes has been described in detail elsewhere [65–68].

The J values of the dinuclear complexes were determined by calculating the energy difference between the high spin state (E_{HS}) and broken symmetry state (E_{BS}), according to the following equation:

$$J = \frac{E_{LS} - E_{HS}}{2S_1S_2 + S_2} \quad (8)$$

where S_1 and S_2 are the local spins for each metal centre and $S_1 > S_2$.

5. Conclusions

We have demonstrated that the Mannich-type ligand H_2L (N,N' -dimethyl- N,N' -bis(2-hydroxy-3-formyl-5-bromo-benzyl)ethylenediamine), with high backbone flexibility and inner N_2O_2 and outer O_4 coordination sites, allows the preparation of a series of dinuclear $M^{II}-Ln^{III}$ complexes. In this complexes, the M^{II} ions occupy the internal coordination sites whereas the oxophilic Ln^{III} ions occupy the external coordination sites, leading to acetate-diphenoxo triply bridged dinuclear complexes $[Cu(\mu-L)(\mu-OAc)Ln(NO_3)_2] \cdot CH_3CN \cdot H_2O$ ($Ln^{III} = Gd, Tb, Dy$ and Er), $[Ni(CH_3CN)(\mu-L)(\mu-OAc)Ln(NO_3)_2] \cdot CH_3CN$ ($Ln^{III} = Nd, Gd, Tb, Dy, Er$ and Y) and $[Co(CH_3CN)(\mu-L)(\mu-OAc)Ln(NO_3)_2] \cdot CH_3CN$ ($Ln^{III} = Gd, Tb, Dy, Er$ and Y). Although the coordination environment of the Ln^{III} ions is similar in all complexes, the Ni^{II} and Co^{II} ions are coordinated to an additional acetonitrile molecule compared to the Cu^{II} -based analogues, which leads into a more twisted disposition of the ligand around the metal ions and an increase in the hinge angle for the former. *dc* magnetic measurements have been carried out in order to study the magnetic exchange interactions between M^{II} and Ln^{III} ions and the results obtained for the Gd^{III} -based complexes have been supported by DFT theoretical calculations. The MCE extracted from the isothermal magnetization curves of the Gd analogues suggests that in these dinuclear systems, the magnetic entropy changes ($-\Delta S_m$) depend more on the magnetic anisotropy than in the total spin and magnetic exchange interactions. Dynamic *ac* magnetic susceptibility measurements show that the $Ni^{II}Dy^{III}$, $Ni^{II}Er^{III}$ and $Co^{II}Dy^{III}$ analogues exhibit slight frequency dependency of the out-of-phase signal at different temperatures, while the $Co^{II}Y^{III}$ analogue displays slow relaxation of the magnetization below $\sim 6-7$ K under an applied field of 1000 Oe.

Supplementary Materials: The following are available online at <https://www.mdpi.com/2312-7481/7/2/22/s1>, Table S1: elemental analysis for complexes 1–15, Table S2: crystallographic data for complexes 1–4, Table S3: crystallographic data for complexes 5–10, Table S4: crystallographic data for complexes 11–15, Table S5: selected bond distances (Å) and angles (°) for complexes 1–4, Table S6: selected bond distances (Å) and angles (°) for complexes 5–15, Table S7: shape measures for Cu^{II} coordination environments in compounds 1–4, Table S8: shape measures for Ni^{II} coordination environments in compounds 5–10, Table S9: shape measures for Co^{II} coordination environments in compounds 11–15, Table S10: shape measures for the LnO_9 coordination environments in compounds 1–15, Figure S1: a perspective view of the structure of 1–4 together with intermolecular hydrogen bonds, Table S11: *Direct current* magnetic data for compounds 1–15, Figure S2: temperature dependence of the $\chi_M T$ product and the difference $\Delta\chi_M T = \chi_M T_{(CuLn)} - \chi_M T_{(ZnLn)}$ for complexes 2–4, Figure S3: temperature dependence of $\chi_M T$ product at 1000 Oe for 6 in the low temperature region. Figure S4: temperature dependence of the $\chi_M T$ product at 1000 Oe and M versus H plot at 2 K for complex 15, Figure S5: M vs. H/T plot for 15, Figure S6: temperature dependence of $\chi_M T$ product at 1000 Oe and M versus H plot at 2 K for 11. Figure S7: temperature dependence of in-phase χ_M' and out-of phase χ_M'' components of the alternating current susceptibility for complexes 8, 9 and 13 under an applied field of 1000 Oe. Figure S8: plot of $\ln(\chi_M''/\chi_M')$ versus $1/T$ at different frequencies for complexes 8, 9 and 13 under an applied field of 1000 Oe, Figure S9: field dependence of the out-of-phase signal vs. frequency at 4 K for 15, Figure S10: Cole–Cole plot for 15, Figure S11: variable-temperature frequency dependency of χ_M'' signal for 15. Figure S12: isothermal field dependent curves for 1, 6 and 11.

Author Contributions: Conceptualization, J.M.S. and E.C.; methodology, I.O.; theoretic calculations, E.S.S.; X-ray crystallography, A.R.-D.; formal analysis, I.O.; investigation, I.O. and E.E.-E.; resources, J.M.S. and E.C.; writing—original draft preparation, I.O. and E.E.-E.; writing—review and editing,

J.M.S. and E.C.; supervision, J.M.S. and E.C.; project administration, I.O.; funding acquisition, J.M.S. and E.C. All authors have read and agreed to the published version of the manuscript.

Funding: This work was supported by the Junta de Andalucía (FQM-195 and the projects of excellence P11-FQM-7756 and A-FQM-172-UGR18), MINECO of Spain (Projects CTQ2014-56312-P and PGC2018-102052-B-C21), the University of Granada and the University of The Basque Country UPV/EHU (Project GIU14/01).

Data Availability Statement: The data presented in this study are available in this article or supplementary material.

Acknowledgments: E.E. and I.O. are grateful to the Government of the Basque Country for their predoctoral and postdoctoral fellowships. The authors acknowledge the technical and human support provided by SGIker of UPV/EHU and European funding (ERDF and ESF).

Conflicts of Interest: The authors declare no conflict of interest.

References

1. Katoh, K.; Komeda, T.; Yamashita, M. The frontier of molecular spintronics based on multiple-decker phthalocyaninato TbIII single-molecule magnets. *Chem. Rec.* **2016**, *16*, 987–1016. [[CrossRef](#)] [[PubMed](#)]
2. McAdams, S.G.; Ariciu, A.-M.; Kostopoulos, A.K.; Walsh, J.P.S.; Tuna, F. Molecular single-ion magnets based on lanthanides and actinides: Design considerations and new advances in the context of quantum technologies. *Coord. Chem. Rev.* **2017**, *346*, 216–239. [[CrossRef](#)]
3. Feng, M.; Tong, M.L. Single ion magnets from 3d to 5f: Developments and strategies. *Chem. Eur. J.* **2018**, *24*, 7574–7594. [[CrossRef](#)]
4. Layfield, R.A. Organometallic single-molecule magnets. *Organometallics* **2014**, *33*, 1084–1099. [[CrossRef](#)]
5. Woodruff, D.N.; Winpenny, R.E.P.; Layfield, R.A. Lanthanide single-molecule magnets. *Chem. Rev.* **2013**, *113*, 5110–5148. [[CrossRef](#)]
6. Escalera-Moreno, L.; Baldoví, J.J.; Gaita-Ariño, A.; Coronado, E. Spin states, vibrations and spin relaxation in molecular nanomagnets and spin qubits: A critical perspective. *Chem. Sci.* **2018**, *9*, 3265–3275. [[CrossRef](#)]
7. Gatteschi, D.; Sessoli, R.; Villain, J. *Molecular Nanomagnets*; Oxford University Press: Oxford, UK, 2007.
8. Clérac, R.; Winpenny, R.E.P. Single-molecule magnets and related phenomena. *Struct. Bond.* **2016**, *172*, 35–48. [[CrossRef](#)]
9. *Lanthanides and Actinides in Molecular Magnetism*; Layfield, R.A.; Murugesu, M. (Eds.) Wiley-VCH: Weinheim, Germany, 2015.
10. Tang, J.; Zhang, P. *Lanthanide Single Molecule Magnets*; Springer: Berlin/Heidelberg, Germany, 2015.
11. Langley, S.K.; Wielechowski, D.P.; Vieru, V.; Chilton, N.F.; Moubaraki, B.; Abrahams, B.F.; Chibotaru, L.F.; Murray, K.S. A {Cr^{III}₂Dy^{III}₂} single-molecule magnet: Enhancing the blocking temperature through 3d magnetic exchange. *Angew. Chem. Int. Ed.* **2013**, *52*, 12014–12019. [[CrossRef](#)]
12. Langley, S.K.; Wielechowski, D.P.; Vieru, V.; Chilton, N.F.; Moubaraki, B.; Chibotaru, L.F.; Murray, K.S. Modulation of slow magnetic relaxation by tuning magnetic exchange in {Cr₂Dy₂} single molecule magnets. *Chem. Sci.* **2014**, *5*, 3246–3256. [[CrossRef](#)]
13. Chandra Mondal, K.; Sundt, A.; Lan, Y.; Kostakis, G.E.; Waldmann, O.; Ungur, L.; Chibotaru, L.F.; Anson, C.E.; Powell, A.K. Single-molecule magnets coexistence of distinct single-ion and exchange-based mechanisms for blocking of magnetization in a Co^{II}₂Dy^{III}₂ single-molecule magnet. *Angew. Chem. Int. Ed.* **2012**, *51*, 7550–7554. [[CrossRef](#)]
14. Gupta, T.; Beg, M.F.; Rajaraman, G. Role of single-ion anisotropy and magnetic exchange interactions in suppressing zero-field tunnelling in {3d-4f} single molecule magnets. *Inorg. Chem.* **2016**, *55*, 11201–11215. [[CrossRef](#)] [[PubMed](#)]
15. Reis, M.S. Magnetocaloric and barocaloric effects of metal complexes for solid state cooling: Review, trends and perspectives. *Coord. Chem. Rev.* **2020**, *417*, 213357. [[CrossRef](#)]
16. Oyarzabal, I.; Artetxe, B.; Rodríguez-Diéguez, A.; García, J.Á.; Seco, J.M.; Colacio, E. A family of acetato-diphenoxo triply bridged dimetallic Zn^{II}Ln^{III} complexes: SMM behavior and luminescent properties. *Dalton Trans.* **2016**, *45*, 9712–9726. [[CrossRef](#)] [[PubMed](#)]
17. Llunell, M.; Casanova, D.; Cirera, J.; Bofill, J.M.; Alemany, P.; Alvarez, S.; Pinsky, M.; Avnir, D. *SHAPE*; v1.1b; Universitat de Barcelona: Barcelona, Spain, 2005.
18. Chilton, N.F.; Anderson, R.P.; Turner, L.D.; Soncini, A.; Murray, K.S. PHI: A powerful new program for the analysis of anisotropic monomeric and exchange-coupled polynuclear d- and f-block complexes. *J. Comput. Chem.* **2013**, *34*, 1164–1175. [[CrossRef](#)]
19. Rajeshkumar, T.; Annadata, H.V.; Evangelisti, M.; Langley, S.K.; Chilton, N.F.; Murray, K.S.; Rajaraman, G. Theoretical studies on polynuclear {Cu^{II}₅Gd^{III}_n} clusters (n = 4, 2): Towards understanding their large magnetocaloric effect. *Inorg. Chem.* **2015**, *54*, 1661–1670. [[CrossRef](#)]
20. Rajaraman, G.; Totti, F.; Bencini, A.; Caneschi, A.; Sessoli, R.; Gatteschi, D. Density functional studies on the exchange interaction of a dinuclear Gd(III)–Cu(II) complex: Method assessment, magnetic coupling mechanism and magneto-structural correlations. *J. Chem. Soc. Dalton Trans.* **2009**, 3153–3161. [[CrossRef](#)]
21. Mahapatra, P.; Koizumi, N.; Kanetomo, T.; Ishida, T.; Ghosh, A. A series of Cu^{II}-Ln^{III} complexes of an N₂O₃ donor asymmetric ligand and a possible Cu^{II}-Tb^{III} SMM candidate in no bias field. *New J. Chem.* **2019**, *43*, 634–643. [[CrossRef](#)]

22. Costes, J.P.; Dahan, F.; Dupuis, A.; Laurent, J.-P. Nature of the magnetic interaction in the (Cu²⁺, Ln³⁺) pairs: An empirical approach based on the comparison between homologous (Cu²⁺, Ln³⁺) and (Ni_{LS}²⁺, Ln³⁺) complexes. *Chem. Eur. J.* **1998**, *4*, 1616–1620. [[CrossRef](#)]
23. Costes, J.P.; Dahan, F.; Vendier, L.; Shova, S.; Lorusso, G.; Evangelisti, M. Ni^{II}-Ln^{III} complexes with: O-vanillin as the main ligand: Syntheses, structures, magnetic and magnetocaloric properties. *Dalton Trans.* **2018**, *47*, 1106–1116. [[CrossRef](#)] [[PubMed](#)]
24. Colacio, E.; Ruiz, J.; Mota, A.J.; Palacios, M.A.; Cremades, E.; Ruiz, E.; White, F.J.; Brechin, E.K. Family of carboxylate- and nitrate-diphenoxo triply bridged dinuclear Ni^{II}Ln^{III} complexes (Ln = Eu, Gd, Tb, Ho, Er, Y): Synthesis, experimental and theoretical magneto-structural studies, and single-molecule magnet behavior. *Inorg. Chem.* **2012**, *51*, 5857–5868. [[CrossRef](#)]
25. Roy, S.; Oyarzabal, I.; Vallejo, J.; Cano, J.; Colacio, E.; Bauza, A.; Frontera, A.; Kirillov, A.M.; Drew, M.G.B.; Das, S. Two polymorphic forms of a six-coordinate mononuclear cobalt(II) complex with easy-plane anisotropy: Structural features, theoretical calculations, and field-induced slow relaxation of the magnetization. *Inorg. Chem.* **2016**, *55*, 8502–8513. [[CrossRef](#)]
26. Chandrasekhar, V.; Dey, A.; Mota, A.J.; Colacio, E. Slow magnetic relaxation in Co(III)–Co(II) mixed-valence dinuclear complexes with a Co^{II}O₅ X (X = Cl, Br, NO₃) distorted-octahedral coordination sphere. *Inorg. Chem.* **2013**, *52*, 4554–4561. [[CrossRef](#)] [[PubMed](#)]
27. Modak, R.; Mondal, B.; Sikdar, Y.; Banerjee, J.; Colacio, E.; Oyarzabal, I.; Cano, J.; Goswami, S. Slow magnetic relaxation and water oxidation activity of dinuclear Co^{II}Co^{III} and unique triangular Co^{II}Co^{II}Co^{III} mixed-valence complexes. *Dalton Trans.* **2020**, *49*, 6328–6340. [[CrossRef](#)]
28. Colacio, E.; Ruiz, J.; Mota, A.J.; Palacios, M.A.; Ruiz, E.; Cremades, E.; Hänninen, M.M.; Sillanpää, R.; Brechin, E.K. Co^{II}Ln^{III} dinuclear complexes (Ln^{III} = Gd, Tb, Dy, Ho and Er) as platforms for 1,5-dicyanamide-bridged tetranuclear Co^{II}Ln^{III}₂ complexes: A magneto-structural and theoretical study. *C. R. Chim.* **2012**, *15*, 878–888. [[CrossRef](#)]
29. Basak, D.; van Leusen, J.; Gupta, T.; Kögerler, P.; Bertolasi, V.; Ray, D. Unusually distorted pseudo-octahedral coordination environment around Co^{II} from thioether Schiff base ligands in dinuclear [CoLn] (Ln = La, Gd, Tb, Dy, Ho) complexes: Synthesis, structure, and understanding of magnetic behavior. *Inorg. Chem.* **2020**, *59*, 2387–2405. [[CrossRef](#)]
30. Costes, J.P.; Dahan, F.; Dupuis, A.; Laurent, J.P. Une famille originale de complexes hétérodinucléaires Co(II)-Ln(III): Synthèse et étude magnétostructurale. *C. R. Acad. Sci. Ser. IIc Chem.* **1998**, *1*, 417–420. [[CrossRef](#)]
31. Costes, J.-P.; Dahan, F.; García-Tojal, J. Dinuclear Co^{II}/Gd^{III} and Co^{III}/Gd^{III} complexes derived from hexadentate Schiff bases: Synthesis, structure, and magnetic properties. *Chem. Eur. J.* **2002**, *8*, 5430–5434. [[CrossRef](#)]
32. Zhao, X.Q.; Wang, J.; Bao, D.X.; Xiang, S.; Liu, Y.J.; Li, Y.C. The ferromagnetic [Ln₂Co₆] heterometallic complexes. *Dalton Trans.* **2017**, *46*, 2196–2203. [[CrossRef](#)]
33. Watanabe, A.; Yamashita, A.; Nakano, M.; Yamamura, T.; Kajiwara, T. Multi-path magnetic relaxation of mono-dysprosium(III) single-molecule magnet with extremely high barrier. *Chem. Eur. J.* **2011**, *17*, 7428–7432. [[CrossRef](#)] [[PubMed](#)]
34. Kajiwara, T.; Nakano, M.; Takahashi, K.; Takaishi, S.; Yamashita, M. Structural design of easy-axis magnetic anisotropy and determination of anisotropic parameters of Ln^{III}-Cu^{II} single-molecule magnets. *Chem. Eur. J.* **2011**, *17*, 196–205. [[CrossRef](#)]
35. Maeda, M.; Hino, S.; Yamashita, K.; Kataoka, Y.; Nakano, M.; Yamamura, T.; Kajiwara, T. Correlation between slow magnetic relaxation and the coordination structures of a family of linear trinuclear Zn(II)-Ln(III)-Zn(II) complexes (Ln = Tb, Dy, Ho, Er, Tm and Yb). *Dalton Trans.* **2012**, *41*, 13640–13648. [[CrossRef](#)] [[PubMed](#)]
36. Liu, J.L.; Chen, Y.C.; Zheng, Y.Z.; Lin, W.Q.; Ungur, L.; Wernsdorfer, W.; Chibotaru, L.F.; Tong, M.L. Switching the anisotropy barrier of a single-ion magnet by symmetry change from quasi-D_{5h} to quasi-O_h. *Chem. Sci.* **2013**, *4*, 3310–3316. [[CrossRef](#)]
37. Titos-Padilla, S.; Ruiz, J.; Herrera, J.M.; Brechin, E.K.; Wernsdorfer, W.; Lloret, F.; Colacio, E. Dilution-triggered SMM behavior under zero field in a luminescent Zn₂Dy₂ tetranuclear complex incorporating carbonato-bridging ligands derived from atmospheric CO₂ fixation. *Inorg. Chem.* **2013**, *52*, 9620–9626. [[CrossRef](#)]
38. Colacio, E.; Ruiz, J.; Ruiz, E.; Cremades, E.; Krzystek, J.; Carretta, S.; Cano, J.; Guidi, T.; Wernsdorfer, W.; Brechin, E.K. Slow magnetic relaxation in a Co^{II}-Y^{III} single-ion magnet with positive axial zero-field splitting. *Angew. Chem. Int. Ed.* **2013**, *52*, 9130–9134. [[CrossRef](#)] [[PubMed](#)]
39. Palacios, M.A.; Titos-Padilla, S.; Ruiz, J.; Herrera, J.M.; Pope, S.J.A.; Brechin, E.K.; Colacio, E. Bifunctional Zn^{II}Ln^{III} dinuclear complexes combining field induced SMM behavior and luminescence: Enhanced NIR lanthanide emission by 9-anthracene carboxylate bridging ligands. *Inorg. Chem.* **2014**, *53*, 1465–1474. [[CrossRef](#)]
40. Evangelisti, M.; Brechin, E.K. Recipes for enhanced molecular cooling. *Dalton Trans.* **2010**, *39*, 4672–4676. [[CrossRef](#)] [[PubMed](#)]
41. Sharples, J.W.; Collison, D. Coordination compounds and the magnetocaloric effect. *Polyhedron* **2013**, *54*, 91–103. [[CrossRef](#)]
42. Liu, J.-L.; Chen, Y.-C.; Guo, F.-S.; Tong, M.L. Recent advances in the design of magnetic molecules for use as cryogenic magnetic coolants. *Coord. Chem. Rev.* **2014**, *281*, 26–49. [[CrossRef](#)]
43. Zheng, Y.Z.; Zhou, G.J.; Zheng, Z.; Winpenny, R.E.P. Molecule-based magnetic coolers. *Chem. Soc. Rev.* **2014**, *43*, 1462–1475. [[CrossRef](#)]
44. Pavlishchuk, A.V.; Pavlishchuk, V.V. Principles for Creating “Molecular refrigerators” derived from gadolinium(III) coordination compounds: A review. *Theor. Exp. Chem.* **2020**, *56*, 1–25. [[CrossRef](#)]
45. Colacio, E.; Ruiz, J.; Lorusso, G.; Brechin, E.K.; Evangelisti, M. A ferromagnetically coupled diphenoxo-bridged Gd³⁺-Mn²⁺ dinuclear complex with a large magneto-caloric effect. *Chem. Commun.* **2013**, *49*, 3845–3847. [[CrossRef](#)]
46. Dinca, A.S.; Ghirri, A.; Madalan, A.M.; Affronte, M.; Andruh, M. Dodecanuclear [Cu^{II}₆Gd^{III}₆] Nanoclusters as Magnetic Refrigerants. *Inorg. Chem.* **2012**, *51*, 3935–3937. [[CrossRef](#)]

47. Liu, J.-L.; Lin, W.-Q.; Chen, Y.-C.; Gómez-Coca, S.; Aravena, D.; Ruiz, E.; Leng, J.-D.; Tong, M.-L. Cu^{II}-Gd^{III} cryogenic magnetic refrigerants and Cu₈Dy₉ single-molecule magnet generated by in situ reactions of picolinaldehyde and acetylpyridine: Experimental and theoretical study. *Chem. Eur. J.* **2013**, *19*, 17567–17577. [[CrossRef](#)]
48. Zheng, Y.-Z.; Evangelisti, M.; Winpenny, R.E.P. Large magnetocaloric effect in a Wells–Dawson type {Ni₆Gd₆P₆} cage. *Angew. Chem. Int. Ed.* **2011**, *50*, 3692–3695. [[CrossRef](#)]
49. Wang, P.; Shannigrahi, S.; Yakovlev, N.L.; Hor, T.S.A. Facile self-assembly of intermetallic [Ni₂Gd₂] cubane aggregate for magnetic refrigeration. *Chem. Asian J.* **2013**, *8*, 2943–2946. [[CrossRef](#)]
50. Yonemura, M.; Matsumura, Y.; Ohba, M.; Okawa, H.; Fenton, D.E. Template synthesis of phenol-based heterodinucleating macrocycles with dissimilar N(amine)₂O₂ and N(imine)₂O₂ metal-binding sites. *Chem. Lett.* **1996**, *25*, 601–602. [[CrossRef](#)]
51. *CrysAlisPro Software System*; Agilent Technologies UK Ltd.: Oxford, UK, 2012.
52. *Saint Software*; Bruker AXS Inc.: Madison, WI, USA, 2009.
53. Sheldrick, G.M. *SADABS Program for Empirical Adsorption Correction*; University of Göttingen: Göttingen, Germany, 1996.
54. Sheldrick, G.M. *SHELXTL Program for the Solution of Crystal of Structures*; University of Göttingen: Göttingen, Germany, 1993.
55. Astheimer, H.; Haase, W. Direct theoretical ab initio calculations in exchange coupled copper (II) dimers: Influence of structural and chemical parameters in modeled copper dimers. *J. Chem. Phys.* **1985**, *85*, 1427–1432. [[CrossRef](#)]
56. Noodleman, L. Valence bond description of antiferromagnetic coupling in transition metal dimers. *J. Chem. Phys.* **1981**, *74*, 5737–5743. [[CrossRef](#)]
57. Noodleman, L.; Li, J.; Zhao, X.G.; Richardson, W.H. Density Functional Studies of Spin Coupled Transition Metal Dimer and Tetramer Complexes. In *Density Functional Methods: Applications in Chemistry and Materials Science*; Springborg, M., Ed.; John Wiley and Sons: New York, NY, USA, 1997; pp. 149–188.
58. Becke, A.D. Density-functional thermochemistry. III. The role of exact exchange. *J. Chem. Phys.* **1993**, *98*, 5648–5652. [[CrossRef](#)]
59. Lee, C.; Yang, W.; Parr, R.G. Development of the Colle-Salvetti correlation-energy formula into a functional of the electron density. *Phys. Rev. B* **1988**, *37*, 785–789. [[CrossRef](#)]
60. Vosko, S.H.; Wilk, L.; Nusair, M. Accurate spin-dependent electron liquid correlation energies for local spin density calculations: A critical analysis. *Can. J. Phys.* **1980**, *58*, 1200–1211. [[CrossRef](#)]
61. Stephens, P.J.; Devlin, F.J.; Chabalowski, C.F.; Frisch, M.J. Ab Initio calculation of vibrational absorption and circular dichroism spectra using density functional force fields. *J. Phys. Chem.* **1994**, *98*, 11623–11627. [[CrossRef](#)]
62. Frisch, M.J.; Trucks, G.W.; Schlegel, H.B.; Scuseria, G.E.; Robb, M.A.; Cheeseman, J.R.; Scalmani, G.; Barone, V.; Mennucci, B.; Petersson, G.A.; et al. *Gaussian 09 Revision D.01*; Gaussian, Inc.: Wallingford, CT, USA, 2009.
63. Hurley, M.M.; Pacios, L.F.; Christiansen, P.A.; Ross, R.B.; Ermler, W.C. Ab initio relativistic effective potentials with spin-orbit operators. II. K through Kr. *J. Chem. Phys.* **1986**, *84*, 6840–6853. [[CrossRef](#)]
64. Pritchard, B.P.; Altarawy, D.; Didier, B.; Gibson, T.D.; Windus, T.L. New Basis Set Exchange: An Open, Up-to-date Resource for the Molecular Sciences Community. *J. Chem. Inf. Model.* **2019**, *59*, 4814–4820. [[CrossRef](#)]
65. Ruiz, E.; Cano, J.; Alvarez, S.; Alemany, P. Broken symmetry approach to calculation of exchange coupling constants for homobinuclear and heterobinuclear transition metal complexes. *J. Comput. Chem.* **1999**, *20*, 1391–1400. [[CrossRef](#)]
66. Ruiz, E.; Alvarez, S.; Rodríguez-Forteza, A.; Alemany, P.; Pouillon, Y.; Massobrio, C. *Magnetism: Molecules to Materials*; Miller, J.S., Drillon, M., Eds.; Wiley-VCH: Weinheim, Germany, 2001; Volume 2, p. 5572.
67. Ruiz, E.; Rodríguez-Forteza, A.; Cano, J.; Alvarez, S.; Alemany, P. About the calculation of exchange coupling constants in polynuclear transition metal complexes. *J. Comput. Chem.* **2003**, *24*, 982–989. [[CrossRef](#)]
68. Ruiz, E.; Alvarez, S.; Cano, J.; Polo, V. About the calculation of exchange coupling constants using density-functional theory: The role of the self-interaction error. *J. Chem. Phys.* **2005**, *123*, 164110. [[CrossRef](#)]